Wear 504-505 (2022) 204403

Contents lists available at ScienceDirect

Wear

journal homepage: www.elsevier.com/locate/wear

Influence of crystal orientation on twinning in austenitic stainless-steel during single micro-asperity tribology and nanoindentation

Piyush Patil [a,*], Subin Lee [a], Gerhard Dehm [a,**], Steffen Brinckmann [a,b]

[a] Max Planck Institut für Eisenforschung, Düsseldorf, Germany
[b] Institute of Energy and Climate Research (IEK), Forschungszentrum Jülich, Germany

ARTICLE INFO

Keywords:
Materials tribology
Microstructure
Wear
Twinning
Anisotropy

ABSTRACT

Wear induced deformation has been the focus of numerous studies but the fundamental understanding of the influence of wear direction and crystal anisotropy on microstructure evolution has only been handful. We investigate the influence of wear direction on the deformation mechanisms in single grains with {001} and {111} normal orientation. We observe multivariant twin structures below the wear track. The extent of deformation and the twin density are found to be dependent on the wear direction and normal load. This study also addresses why some grains show twinning while others do not show twinning at identical external loads.

1. Introduction

Wear is responsible for the degradation of engineering components such as gears, ball bearing and railway tracks [1]. Wear and the debris produced by wear result in jamming of components, increase in noise and in fatigue of the material leading to the functional and structural failure of the engineering component. Friction, on the other hand, increases the cost of operation. Moreover, higher economic costs and ecological impact are associated with component replacement and the friction losses. The need for more sustainable solutions has pushed tribology research into overdrive in the last decades [2].

In addition to the surface roughness, the near-surface microstructure determines the tribological properties of the component and its applicability for tribological use-cases. Additionally, plasticity induces grain-refinement and the microstructure evolves in the near-surface region during usage. Grain refinement produces a fine-grained microstructure which has superior mechanical and corrosion resistant properties for subsequent loading [3]. The modified surface layer has historically been called differently "Beilby layer" [4] or "tribo-layer". However, the consensus is that this layer has significantly different properties than the bulk material. Hence, it is of importance to fundamentally understand the mechanisms of microstructure evolution during tribology. With such understanding, the initial component usage and explicit technologies can be optimized. However, the deformation mechanisms of a microstructure depend on multiple parameters such as material properties, grain orientation and the loading conditions, as detailed subsequently. This multitude of parameters results in non-trivial dependencies.

These microstructures are referred as tribological-induced microstructures and can be explicitly tailored by processes like shot-peening and Surface Mechanical Attrition Treatment (SMAT) [5], which produce a fine-grained microstructure as a result of severe plastic deformation. Other explicit surface engineering techniques are hard coatings, nitriding and carburizing, which produce a hard layer with different properties (different material in case of hard coating, and severely altered material in case of nitriding and carburizing) on top of the initial material [6]. In this study, we focus on the microstructure evolution of a bulk material and hence refrain from further discussion of explicit surface layers.

The microstructure evolution in surface layers has been studied for various metals such as austenitic steels and Cu, both having a face centered cubic (FCC) crystal structure. In these metals, grain refinement has been observed in the sub-surface region [7]. There are two competing deformation modes which cause the grain refinement: dislocation glide and deformation twinning [8]. The preferred mode depends on various parameters such as i) crystal structure, ii) stacking fault energy (SFE), iii) grain orientation and grain size, iv) loading conditions including strain rate and v) temperature [9]. Twinning usually occurs in crystals with lower symmetry for which the activation criterion of five independent slip systems for deformation may not be possible. This includes hexagonal close-packed (HCP) and body centered

* Corresponding author.
** Corresponding author.
E-mail addresses: p.patil@mpie.de (P. Patil), dehm@mpie.de (G. Dehm).

https://doi.org/10.1016/j.wear.2022.204403
Received 17 January 2022; Received in revised form 31 May 2022; Accepted 3 June 2022
Available online 18 June 2022

cubic (BCC) crystals [10]. Austenitic stainless steels (FCC) have been reported to twin heavily under severe deformation despite having higher crystal symmetry. Generally, austenitic steels with SFE (18–45 mJ/m^2) are reported to deform by twinning, whereas dislocation glide is preferred if SFE exceeds 45 mJ/m^2 [11]. Hadfield austenitic steels [12] have been studied by Karaman et al. [13] and the competing dislocation-twinning mechanisms during deformation were identified in a single crystal. The authors found that also the strain rate and grain orientation play an important role in twinning and the final twin density. The loading direction (e.g. tension/compression) also influence twinning and the resolved shear stress can be calculated for each dislocation slip system as well as for each twin system with the help of Schmid factor for simple loading conditions [14]. Please note that during wear, the stress field is inhomogeneous, and the resolved shear stress depends on the location, the evolved surface topography (pile-up) as well as on the contact shape and friction coefficient, all of which are difficult to identify. In a recent study [15], discrete dislocation dynamic simulations using a flat surface have revealed fundamental aspects of dislocation nucleation and activity during sliding. That study has showed that dislocations form in front of the sliding asperity and dislocation transport depends on the sliding direction, glide plane and Burgers vector orientation.

We chose grains with {111} and {001} normal orientation to investigate the difference between deformation mechanisms under tribological loading because dislocation glide is anisotropic as it occurs on {111} planes and < 110 > directions. By using a grain with {111} normal direction we explore the easy glide direction. On the contrary, we envision that {001} is a more difficult to wear as multiple glide-systems have to interact to accommodate plasticity. We use a spherical diamond indenter to mimic a micro-asperity as a counter body. We investigate the influence of the grain orientation and sliding direction. We observe that even though twinning was prevalent in (010) grains, the twin density is different for different sliding directions.

2. Methods and materials

2.1. Material and sample preparation

Commercial polycrystalline austenitic stainless-steel with the chemical composition as shown in Table 1 is used in this study. The SFE is estimated as 33 mJ/m^2 based on the empirical model proposed by Bellefon et al. [16]. In this SFE evaluation, the contribution of nitrogen is not considered. To ensure that the grains are sufficiently large to conduct wear experiments inside a single grain without grain-boundary interference, the as-received alloy was annealed for one week at 1200 °C. After the heat treatment, the steel was cut by electrical discharge machining into a disk with a diameter and thickness of 20 mm and 3 mm, respectively. Samples were prepared by grinding, polishing with a 3 μm diamond suspension (Struers GmbH) for ~ 10 min and chemo-mechanical polishing for ~ 45 min using a colloidal silica suspension (Struers GmbH). Finally, the samples were cleaned by water. The final average roughness of the samples was 9 ± 1 nm. Roughness measurement was conducted using a confocal microscope (Keyence VK-1000) and analyzed by MultiFileAnalyzer software (Keyence).

2.2. Microstructure analysis by electron microscopy

Scanning electron microscopy (SEM) was used to image the sample surface, while the grain size and grain orientation was determined by electron backscatter diffraction (EBSD). Both evaluations were performed in a SEM (JSM 6490, JEOL) at 15 kV acceleration voltage and very large spot size with 100 μm aperture optimized for larger working distance (WD) ~ 23 mm. The color-coded inverse pole figure (IPF) maps were obtained in the TSL-OIM software (EDAX). Please refer to Supplementary Fig. S1 for the overview IPF-map showing grain size distribution. Datapoints with a confidence index (CI) < 0.1 were excluded in the analysis. Large grains with (010) and (111) orientations were selected for the wear experiments. The EBSD scans inside the wear tracks were executed in a DualBeam FIB-SEM (Scios 2, Thermo Fisher Scientific) at an acceleration voltage of 15 kV, a current of 3.2–6.4 nA and working distance of 13 mm with step size of 50 nm. The diffraction patterns were collected by the EDAX Velocity camera. The EBSD scans were obtained by orienting the wear track vertically to prevent shadowing of the electron beam at the side pile-up.

To examine the cross-section, TEM FIB foils were extracted to the surface from the wear tracks: the TEM foil plane was either perpendicular or parallel to the wear direction. The preparation of the TEM foil was done by first depositing a platinum layer on the surface to protect it from the damage from Ga-ion milling. The TEM foil of ~2 μm thickness and 8 μm depth were cut and extracted from the wear track, and then thinned down to the thickness of ~100–150 nm at 30 kV. The low energy polishing at 5 kV was carried out to reduce the damage and ion implantation. The Transmission Kikuchi Diffraction (TKD) scans were obtained with the same EBSD detector at an acceleration voltage of 30 kV with a current of 6.4 nA and a step size of 5 nm. For advanced characterization, TEM studies were conducted in the JEOL 2200FS and JEOL 2100PLUS which were operated at an acceleration voltage of 200 kV. High resolution TEM (HR-TEM) images were taken using an aberration-corrected TEM (Titan Themis 300, the Thermo Fisher Scientific) operating at 300 kV acceleration voltage.

Twin densities (number of twins per distance) were measured using the line intercept method and intersecting the twins under an angle of 90°. Similarly, the dislocation density was evaluated using the line intersect method with a fixed line pattern for all images. The dislocation density was then calculated using the following equation:

$$\rho = {}^{n}/_{L} \qquad \text{Eq. (1)}$$

where ρ is twin (or dislocation) density, n is the number of twins (or dislocations) intersecting with the line profile and L is the length of the line profile. The provided error value is the standard deviation.

2.3. Scratching and nanoindentation

A nanoindenter (G200, Keysight/Agilent) was used to conduct indentation and wear experiments with a spherical diamond tip (radius: 100 μm) as a micro-asperity against the polished sample. The diamond tip was chosen since diamond is chemically inert while the spherical shape and size of the tip ensures that the deformation region is large and with little surface gradients. Severe surface gradients would obstruct post-deformation inspection.

We produced wear tracks with a ramped-up normal load that increased from 0 to 300 mN while sliding along a 100 μm wear track with a nominal sliding velocity of 10 μm/s inside a large grain. For the (010) grain, we chose [101] as the primary wear direction; this orientation is denoted as (010)[101]. Note that from here onward, we describe the wear track orientation as (normal orientation)[direction of wear]. Afterwards, the wear direction was changed by rotating the sample with respect to the (010) grain normal. The wear experiments were performed in the [001], [40$\bar{1}$] and [$\bar{1}$01] direction by rotating the sample by

Table 1
Chemical composition of Austenitic stainless-steel.

Sample	C	Fe	Cr	Mn	Ni	P	S	Si
Steel	0.005	46.37	24.5	1.73	18.8	0.01	<0.0005	2.33

45°, 60° and 90°, respectively (see Fig. 1). The target angles are hit within the accuracy of 2.5°. Reference nanoindentation was executed with the same tip and normal force inside the same grain. Please refer to Supplementary Fig. S2 for lower magnification SEM image showing wear tracks in different directions.

Wear experiments were performed in (111) grain in similar fashion. There, we chose (111)[$\bar{1}$10] as the principal wear direction and wear experiments were performed in the [$\bar{3}$12] and [10$\bar{1}$] direction by rotating the sample by 45°, and 120° respectively.

3. Results

This section includes three aspects of the investigation: initially, we evaluate twinning in the (010)[101] wear track. Then we present the results of wear tracks in different crystallographic direction and finally, we draw the comparison between indentation and wear deformation in the same grain.

3.1. *Wear in* (010) *grain*

3.1.1. *Wear direction* (010)[101]

The color coded IPF map of the wear track in [101] direction inside the (010) grain is presented in. Fig. 2. The green colored grains in IPF map are identified as twins which indicates a (110) plane normal orientation. In addition, the crystal symbols show the crystallographic orientation change. Based on the orientation of the slip traces, twin planes are either (11$\bar{1}$) or ($\bar{1}$11). The average twin density is ~1.4 × 10^6 twins/m calculated by the line intercept method, which counts the number of twins intersecting the line profile. Since, we only consider the length of the line profile, the density is reported in per unit length rather than area or volume. The twins are spaced equidistantly with a projected distance of 0.45 ± 0.17 μm with an average thickness of 0.31 ± 0.10 μm. This calculation is based on projected twin widths observed on the surface by EBSD.

Please note that there is a smooth orientation gradient inside the wear track as shown by the crystal symbols A and B, the misorientation angle between A and B is ~15.4° and misorientation axis is [10$\bar{1}$]. When compared to the crystal orientation outside of the wear track, the crystal inside the wear track is rotated around the direction perpendicular to the [101] wear direction. Hence, despite the complex stress state, the deformation/lattice rotation is directly attributed to direction of wear.

Fig. 3a) shows the cross-sectional view of the deformed wear track imaged by TKD. The sample was lifted-out from the yellow box in Fig. 2 and has a [10$\bar{1}$] viewing direction. The twins appear smaller in this map than the ones in Fig. 2 which is attributed to 10 times smaller step size, in other words - higher spatial resolution of TKD than EBSD. The twins span across the entire height of the TEM foil, which is ~10 μm. Twinning is distinctly identified in Fig. 3a) and visualized by the crystal symbols A and B corresponding to the matrix and the twinned region, respectively. In addition, the parent grain shows orientation gradient across the height of the scan area as shown in the point to origin misorientation profile, which is plotted along the white arrow (Fig. 3b). This misorientation increases until 0.8 μm below the surface and then decreases towards the bottom of the map. The sharp misorientation steps (60°) denote boundaries between twins and parent grain. The twins are tilted towards the wear direction indicted by the white arrow above the surface (Fig. 3a).

The corresponding bright field TEM (BF-TEM) image of the TEM foil reveals the same primary twin system (Fig. 4) in addition to a second twin system. Diffraction patterns from two different regions were obtained – region A) which is near the surface and B) distant from the surface. The FCC [10$\bar{1}$] diffraction pattern with twin reflections is visible in region B while streaks appear near the sample surface. These streaks are caused by the high strain resulting in grain rotation beneath the wear track.

The presence of multiple twin orientations near the surface suggests more severe plastic deformation in this domain. The density of second twins decreases away from the surface (Fig. 5a) and a magnified HR-TEM image (Fig. 5b). Fig. 5b) shows multiple twin structure consisting of two different twin systems (also called "multivariant twins") which intersect each other and form a complex structure. Since the image is taken in a common [10$\bar{1}$] zone axis, both twin systems are observed edge-on. A quantitative analysis of the twin density is carried out by applying the linear intercept [17] method on cross-section TEM and scanning TEM (STEM) images (see Supplementary Fig. S3 for STEM images). The line profile is drawn perpendicular to the twin boundaries and the number of intersects are counted, the twin density for the two twin systems is calculated individually. The two twin planes are identified as ($\bar{1}$1$\bar{1}$) and (111), where ($\bar{1}$1$\bar{1}$) twins have a twin density of 2.3 ± 0.3 × 10^7 twins/m and the (111) twins have a density of 5.2 ± 0.8 × 10^7 twins/m. The average twin spacing between ($\bar{1}$1$\bar{1}$) twins is 44 ± 5 nm and 20 ± 3 nm for (111) twins. These twins occur often in bundles – clusters of closely spaced twins are separated by larger spacing (see Fig. S3) explaining the reason for large standard deviation value in twin spacing. The widths of the twins are in the range of 2–5 nm, the second twin system - (111) has slightly thinner twins than the primary twin system - ($\bar{1}$1$\bar{1}$). The region near the twin intersection shows strong diffraction contrast indicating high local strains.

In order to complete the understanding of twin microstructure below the wear track, another cross-section TEM foil lift-out was extracted in a way that the normal direction of TEM foil is parallel to the wear direction. Note that this extraction was done from another wear track with symmetric orientation as wear track *I*. (see Fig. 2 for schematic position of lift-out with respect to wear direction and see Supplementary Fig. S4

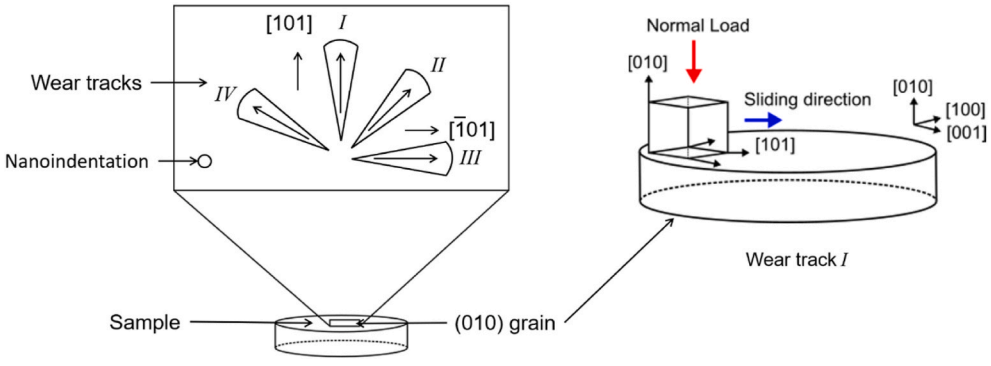

Fig. 1. The schematic of the wear tracks in different directions inside the (010) grain along with nanoindentation. The principal direction is [*101*] and is denoted by the roman numeral *I* while subsequent numerals indicate wear tracks in directions 45, 60, 90°, respectively. An enlarged schematic of wear track *I* describes the grain orientation and wear direction in detail.

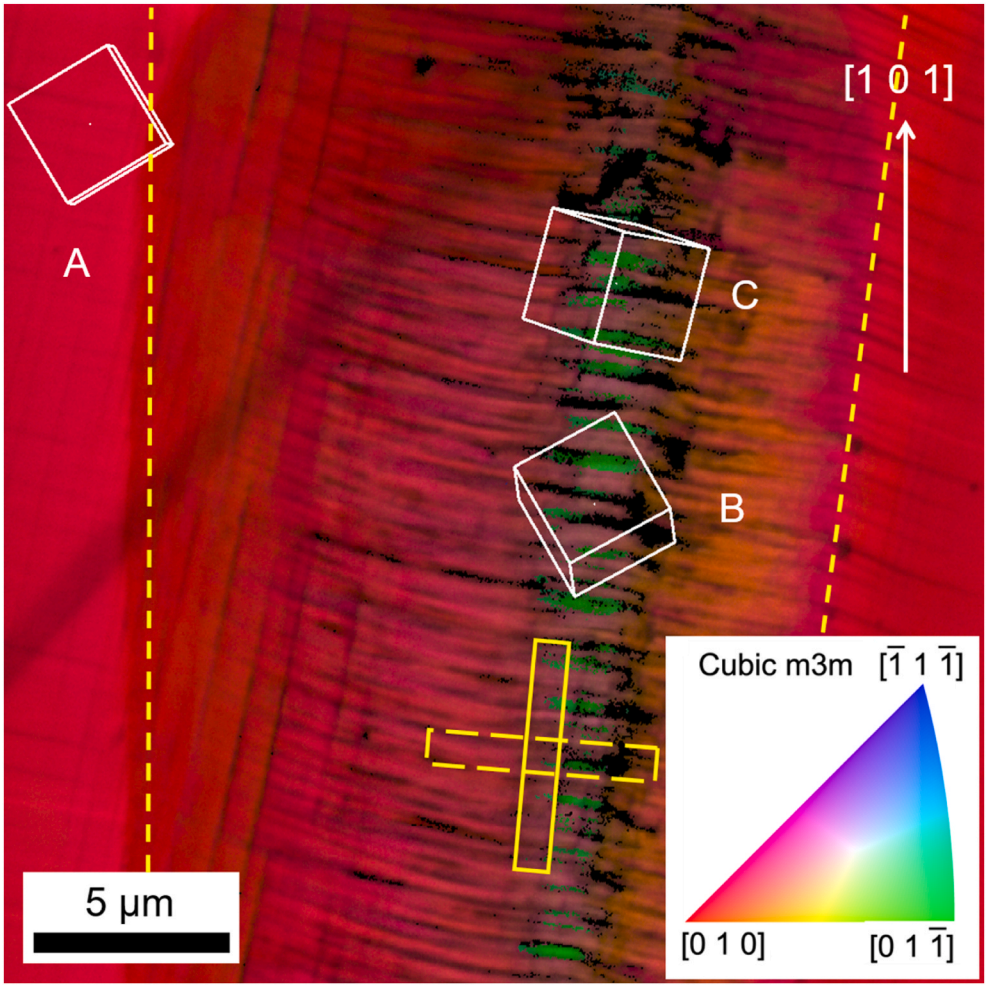

Fig. 2. Color coded IPF in [*001*] sample direction (surface normal) and image quality (IQ) map of the wear track in the direction [*101*] (reference wear track *I* in Fig. 1). A: crystal outside the wear track represents the orientation of the undeformed parent grain. B: crystal inside the wear track shows the orientation of deformed domain. C: crystal of the twinned region. The yellow rectangle with solid line indicates the location and orientation of TEM foil extraction. The yellow rectangle with dashed line represents the schematic position of another cross-section lift-out with respect to the wear direction. The boundary between the wear track and parent grain is marked by a dashed yellow line. (For interpretation of the references to color in this figure legend, the reader is referred to the Web version of this article.)

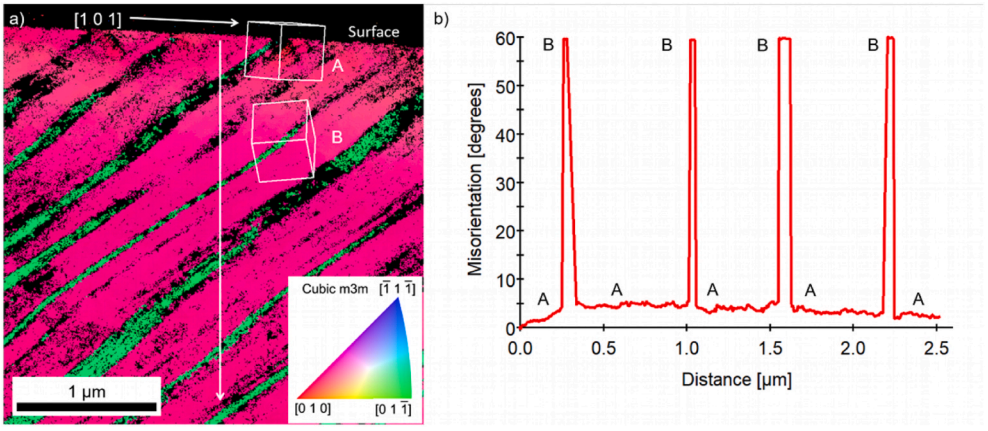

Fig. 3. a) TKD-IPF map of TEM foil cut along the wear direction shown by a white arrow above the surface of the TEM foil. The IPF references the surface normal direction during wear; this direction is the same as in Fig. 2 b) Point to origin misorientation plot along the white arrow pointing downwards in a). The crystal orientations are shown for A: parent grain, B: twinned region.

for IPF-map of the wear track and the site of FIB lift-out). We also carried out the TKD on the respective FIB TEM foil and the results are shown in Fig. 6. From the IPF-map, the twin density appears to decrease away from the surface. The twins belong to the (111) or $(\bar{1}1\bar{1})$ twin system. Please note that we do not observe the twins edge-on from this orientation.

Since the twins were not observed edge-on in this TEM foil, their projected width which is in the range of 13–15 nm overestimates their real width. With the help of Figs. 2, 3 and 6, a 3-dimensional schematic was drawn to illustrate the microstructure below the wear track in [101] direction, please refer to the supplementary information (See Fig. S5).

In summary, twin density measurements by EBSD underestimates the more accurate twin density values (as measured by TEM) by a factor of 10.

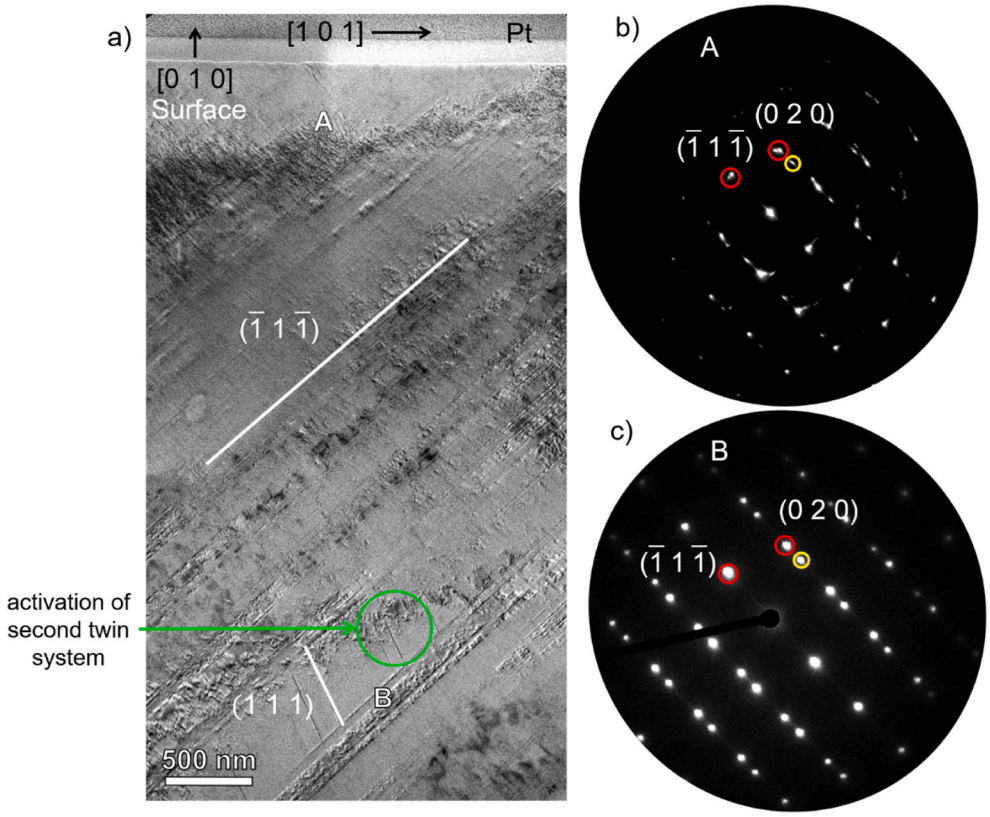

Fig. 4. BF-TEM image (a) and diffraction patterns (b,c) from two different regions below the wear track indicating presence of twin structure. The wear direction [*101*] and surface orientation [*010*] are shown by black arrows. b) Diffraction pattern from the region near to the surface of the wear track. c) Diffraction pattern from the region distant to the surface. The reflections highlighted by red circles are from the austenite matrix while yellow indicates a reflection from twins. Note that a second twin system is activated (see green circle). (For interpretation of the references to color in this figure legend, the reader is referred to the Web version of this article.)

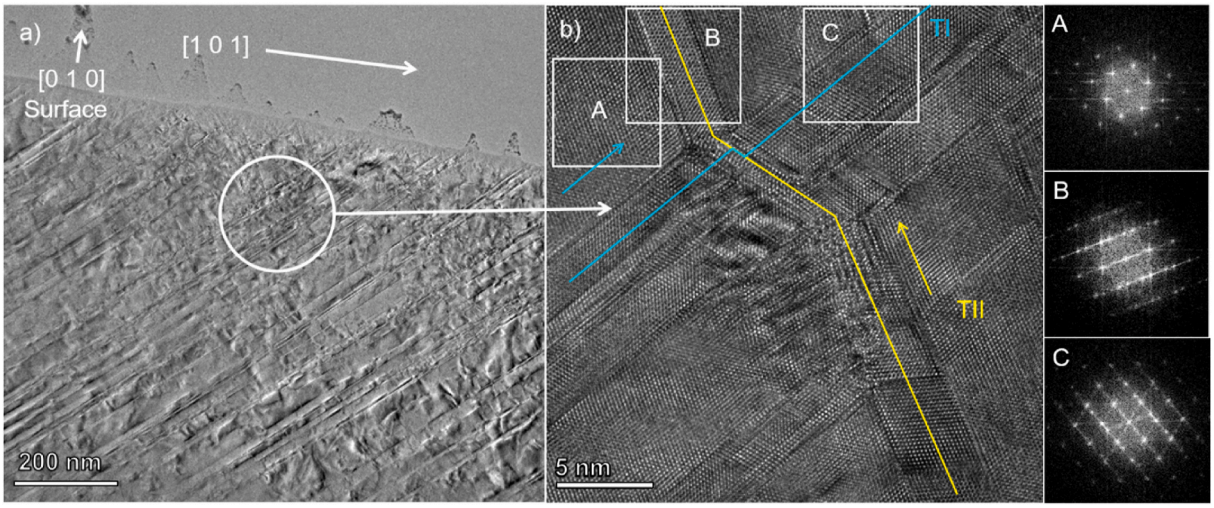

Fig. 5. a) BF-TEM image taken from the area below the wear track, which runs along [101] direction b) Magnified high resolution image from the highlighted area in a). TI and TII denote two distinct twin systems. The corresponding fast Fourier transformation (FFT) images of regions A, B and C reveal the matrix, TII and TI respectively.

3.1.2. *Wear direction* (010)[1̄01]

Fig. 7 shows an IPF-map of a wear track performed in the direction [1̄01] (wear track *III* in Fig. 1) which is 90° to the (010)[101] wear track (or wear track *I* in Fig. 1). Both directions are crystallographically equivalent.

The twinning behavior and wear track morphology for wear track *III* are similar to the (010)[101] wear track, which is shown in Fig. 2. In both wear tracks, the twins are periodic (see Figs. 2 and 7). The twin density measured by EBSD in case of this wear track is ~1.4 × 10^6 twins/m. Note that there is virtually no difference in this value compared to the value reported for the wear track *I*. In Fig. 7, the orientation of the slightly deformed parent grain is highlighted by crystal symbol A, while B indicates the severely deformed region and C highlights the twin region. The misorientation between A and B is 16.8° and its misorientation axis is [337]. The misorientation axis shows that the orientation change does not occur along the wear direction, unlike in wear track *I* (Fig. 2).

3.1.3. *Wear direction* (010)[001]

Fig. 8 shows the IPF map from an EBSD scan on the wear track performed in (010)[001] direction (ref. wear track *II* in Fig. 1). It does not

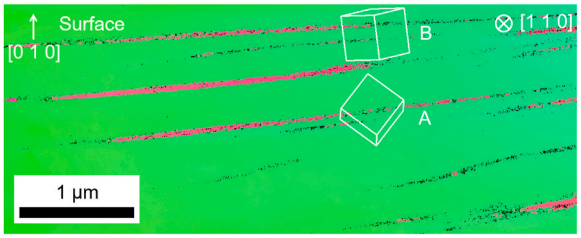

Fig. 6. IPF orientation map of the cross-section sample obtained by TKD. Wear direction $(001)[110]$ is parallel to the surface normal of the TEM foil. The orientations are represented by crystal B: parent grain, A: twin region.

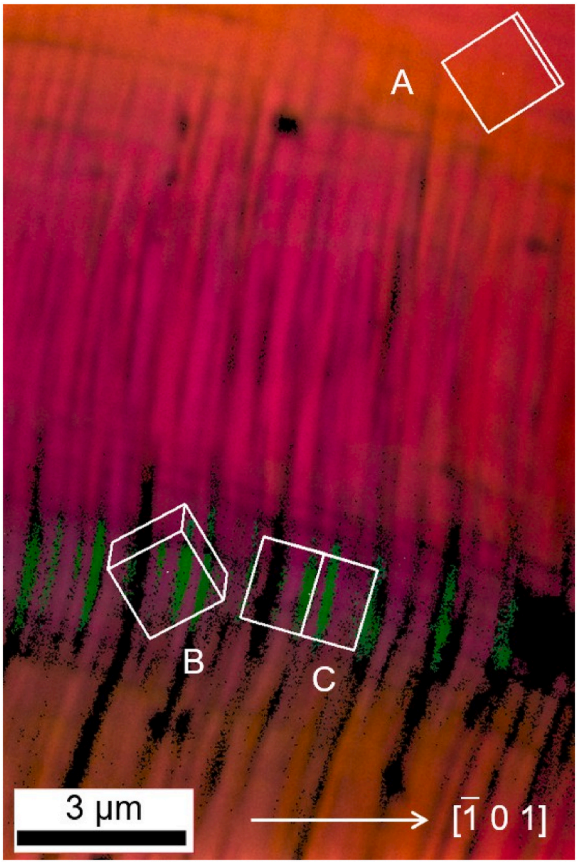

Fig. 7. Twin pattern as observed inside the wear track after rotating the sample by 90° clockwise to the principal direction (ref. wear track *III* in Fig. 1). A: crystal orientation representing slightly deformed parent grain inside wear track. B: crystal orientation inside the wear track shows severely deformed region. C: crystal orientation of the twinned region.

resolve any twin grain formation on the surface but a peculiar morphology is observed. Fig. 9 shows the BF-TEM image from a TEM foil prepared from the region indicated in Fig. 8. TEM analysis clearly shows the presence of twins with similar structure to the TEM foil from the wear tracks performed in $(010)[001]$ direction (Fig. 4). From Figs. 8 and 9 we can estimate that at least three twin systems are present under the wear track, and it is plausible that a fourth twin system could be present but remains obscure for this TEM foil orientation.

The twins inclined to the surface belong to the $(\bar{1}1\bar{1})$ twin system while the twins parallel to the surface could belong to either $(\bar{1}\bar{1}1)$ or $(1\bar{1}\bar{1})$ twin systems. Because of very low number of $(\bar{1}1\bar{1})$ twins, the twin density is not reported. The distance between the twins in Fig. 9b) is approximately 800 nm. The $(\bar{1}\bar{1}1)$/ $(1\bar{1}\bar{1})$ twins are not edge on hence the twin density and spacing values are not reported. Note that the twin

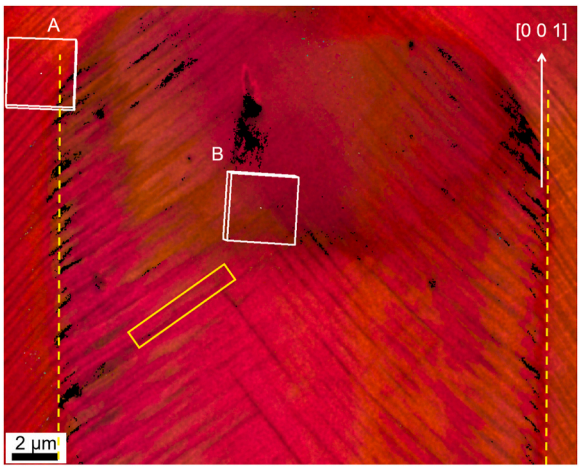

Fig. 8. IPF map of the wear track performed in $(010)[001]$ direction by rotating the sample by 45° relative to the primary wear direction. A: Crystal orientation of undeformed parent grain, B: Crystal orientation inside the wear track. It shows no indication of twinning on the surface in the IPF-map. The rectangle shows the location and orientation of a TEM foil cut out from the track as analyzed in Fig. 9. Boundary between undeformed region and wear track is marked by yellow line. (For interpretation of the references to color in this figure legend, the reader is referred to the Web version of this article.)

spacing below the $(010)[001]$ wear track appears significantly higher than the twin spacing below the $(010)[101]$ wear track.

3.2. *Wear track on a* (111) *grain* $(111)[\bar{1}10]$

In this section we report the results of wear in the (111) grain. Here, we focus on the wear track in the $[\bar{1}10]$ direction. IPF maps of the wear tracks in other directions are provided in the supplementary figures (see Fig. S6).

The FIB lift-out was obtained from the region highlighted in Fig. 10 a). The BF-TEM image shows a planar fault contrast as indicated by the yellow line in Fig. 10 b), however the $[\bar{1}10]$ zone axis diffraction pattern in Fig. 10 c) shows no indication of twins. Instead, TEM reveals that a dislocation network has formed by interaction of two slip systems. The dislocation density was measured for Fig. 10 b) using the linear intercept method (please refer to supplementary Fig. S7 for line profiles used for the calculation), which provides the upper limit for the dislocation density as $1.6 \pm 0.8 \times 10^{14}/m^2$.

3.3. *Indentation in* (010) *grain*

To distinguish the microstructural changes due to wear from those due to indentation, we carried out the indentation experiment in the same grain as the wear tracks. Fig. 11 a) shows the IPF-map of the indent and the highlighted region from where the FIB TEM foil was taken out. The BF-TEM image is shown in Fig. 11 b). In this configuration, twin structures would be observed from $[101]$ zone axis, but Fig. 11 c) shows no indication of twinning suggesting that dislocation slip is the dominant deformation mechanism. To ensure that there were indeed not twins, another FIB TEM foil was extracted perpendicular to the one shown in Fig. 11. Also, this TEM foil does not reveal any twin microstructure, as shown in the supplement material (Fig. S8).

We also determined the dislocation density of $9.4 \pm 2.0 \times 10^{13}/m^2$ after indentation (see Fig. S8).

4. Discussion

In this section, we discuss the results in three sections: 1. Twinning as a preferred mode of deformation as opposed to dislocation plasticity, 2.

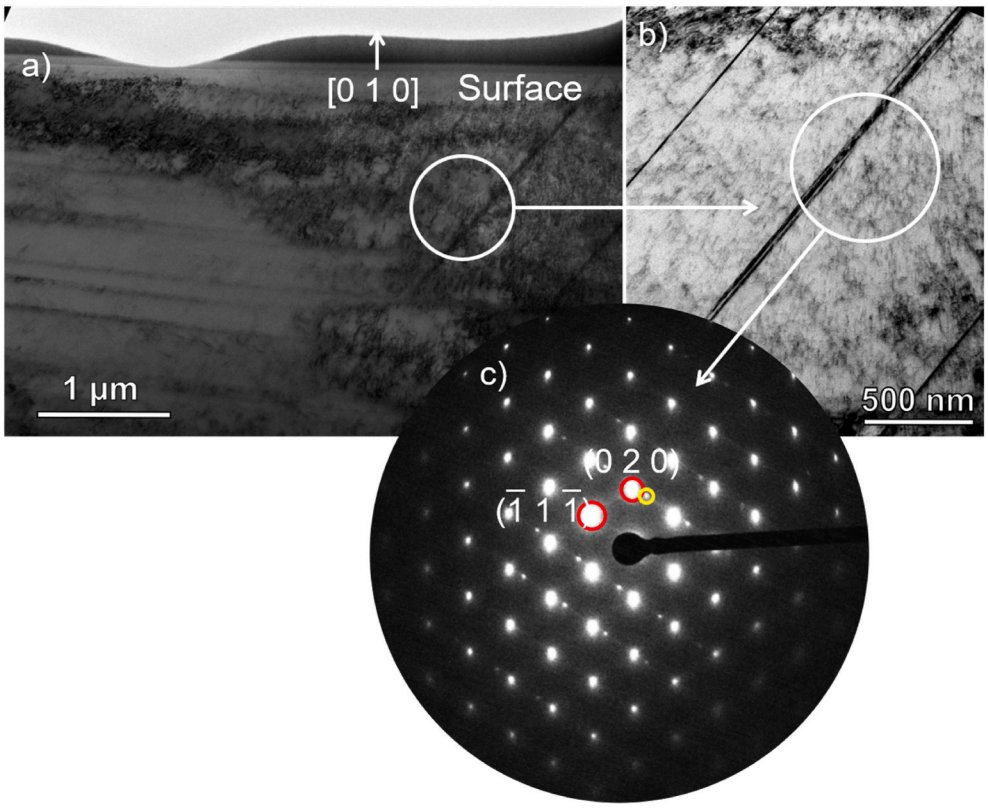

Fig. 9. a) BF-TEM image taken from the $(010)[001]$ wear track. It shows nanotwins below the wear track, surface orientation [010] is represented by white arrow b) BF-TEM image taken at $[10\bar{1}]$ zone axis at higher magnification; c) shows the corresponding diffraction pattern with a twin reflection highlighted by a yellow circle. (For interpretation of the references to color in this figure legend, the reader is referred to the Web version of this article.)

influence of the wear direction on the twin density and 3.rmation of multivariant twin microstructures.

4.1. Deformation in indentation and in wear fo

Mechanical twinning is more favorable in metals with low stacking fault energy. Austenitic stainless steels with the SFE in the range of 18–45 mJ/m2 generally exhibit twinning [11]. The present metal has a SFE in that range and exhibits twinning under certain loading conditions. Generally, we observed the presence of dislocation plasticity and the absence of twinning after indentation with a spherical tip in a (010) grain. This finding is in line with a previous study [18], in which dislocation plasticity (not twinning) occurred during spherical indentation and was evaluated by EBSD. However, those authors found twinning during tensile deformation of the Ni-enriched AISI 304 Austenitic stainless steel. Contrary, Seo et al. [19] used a Berkovich tip for nanoindentation and observed twinning as a primary mode of deformation in (010) grains. This difference in nanoindentation deformation response could be caused by the tip geometry as the Berkovich tip results in higher strain accumulation below the center of the indent than the spherical tip.

We observe twinning during some scratch experiments, but not during indentation although both experienced the same external force, and the same indenter was used. When indenting a (010) grain with a spherical indenter tip, we observe no twins with neither EBSD nor with TEM based methods. In TEM, we investigated two orthogonal TEM foil to ensure that we did not miss twinning due to invisibility criteria. On the other hand, we observe twinning after scratching even with coarse EBSD method. Therefore, we conclude that wear results in twinning in cases where indentation does not. This finding is in agreement with [3], which showed that in indentation, twinning is not observed while other modes of deformation which have a higher shear/tensile component - result in twinning [10].

The twin nucleation is facilitated when the shear stress on a twin system reaches a threshold, i.e., critical resolved shear stress (CRSS) for twinning. There are many factors that influence the CRSS for twinning during indentation and tribology: the 3-dimensional stress state, type of indenter tip, crystallographic orientation. These factors make it nearly impossible to estimate the CRSS for this alloy by nanoindentation let alone by tribology. Therefore, we do not focus on quantifying CRSS value in this study but compare phenomenological the deformation mechanisms. Regarding the present indentation results, the CRSS for twinning is not attained, yet dislocation slip is activated on at least 3 slip systems on which a dense dislocation network is formed in the (010) grain, as shown in Fig. 11.

One of the factors influencing wear deformation could be oxide formation on the surface as austenite forms few nanometers thick layer of oxide on the surface but considering microscale deformation in this work, we believe the effect would be negligible as the oxide layer in inspected regions appear continuous and without cracks. The oxide layer could influence the friction coefficient and material adhesion. These factors do not play a role in this study as we do not measure/analyze the friction coefficient and because we use an inert diamond tip as a counterbody, respectively. Please refer to Supplementary Fig. S9 for STEM-BF image and EDX analysis on the oxide layer.

The shear component during wear facilitates the activation of twinning. The extent of deformation in terms of twin size, twin-spacing and number of twin systems activated varies depending on the wear direction since changing the wear direction effectively changes the shear direction on the crystal and changes how the shear force is resolved on each twin system. These relations are discussed in the next section.

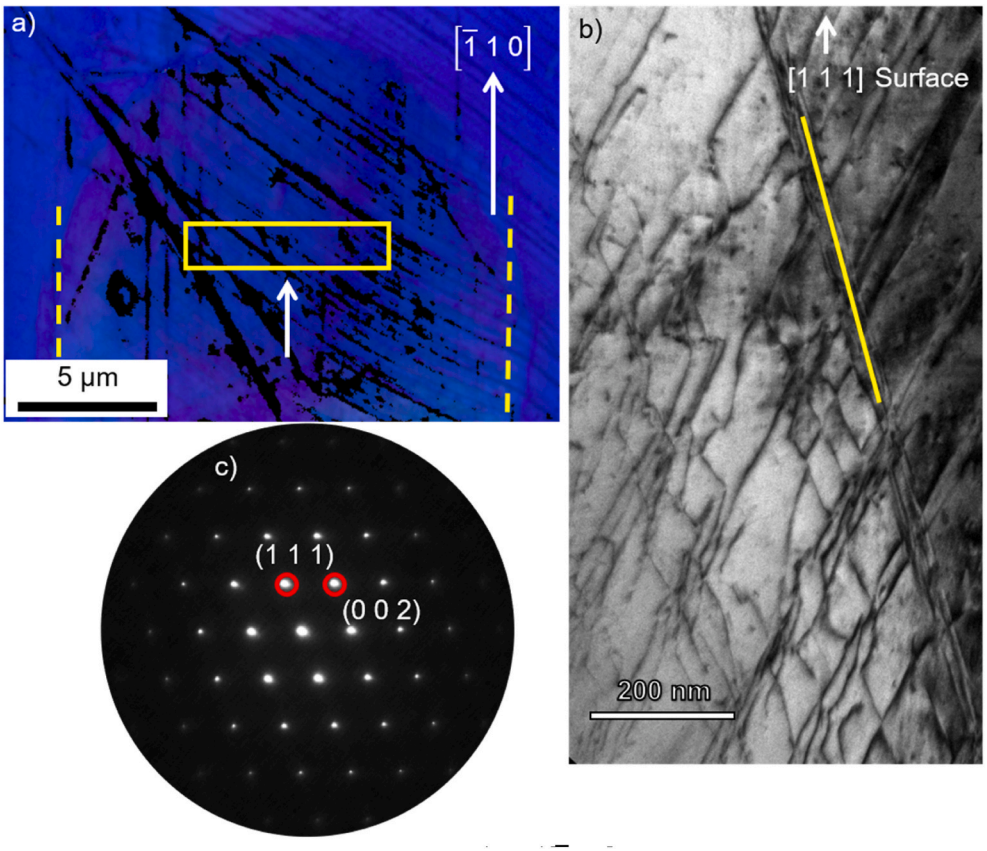

Fig. 10. a) IPF map of the wear performed in $(111)[\bar{1}10]$. b) BF-TEM image from the region indicated in the IPF map in a). Yellow line highlights a stacking fault. c) diffraction pattern from the region highlighted in image b) taken at $[\bar{1}10]$ zone axis. (For interpretation of the references to color in this figure legend, the reader is referred to the Web version of this article.)

4.2. Influence of wear direction

By changing the wear direction, we change the direction of the friction force and consequently, the CRSS on the different twinning systems. Fig. 2 shows the twin microstructure formed inside (010)[101] wear track. Although, the twins are easily distinguishable in the IPF-map of the (010)[101]wear track, the further analysis by TKD and TEM (Figs. 3 and 4) shows that the twins are thinner and more dense than evaluated by EBSD. For the (010)[001] wear track (Fig. 8), the twins cannot be identified by EBSD but the TEM analysis shows the presence of narrow twins. This measurement artifact of EBSD is attributed to the large excited volume (or lower spatial resolution) [20] for diffracted (backscattered) electrons compared to TKD, TEM and HR-TEM as well as indexing only the result for the most prominent Kikuchi pattern as opposed to displaying all reflections in selected area diffraction for TEM. Thus, for TEM even weak reflections from the twins can be resolved in the diffraction pattern. Hence, deformation twinning can be missed when depending solely on automated SEM-EBSD based characterization.

The sliding directions of wear track *I* (Fig. 2) and wear track *III* (Fig. 7) are 90° to each other and show identical wear track morphology, twin shape as well as twin density (~1.4×10^6 twins/m). This is due to the four-fold symmetry of the FCC crystal as the planes on which resolved shear stresses act are also rotationally symmetrical. The rather low twin density in the (010)[001] wear track compared to (010)[101] wear track (twin density: $2.3 \pm 0.3 \times 10^7$ twins/m) is due to different sliding direction. Also note that, twinning is not observed in (111) grain in EBSD as well as in TEM investigations. Hence, while EBSD significantly misquantifies the twin spacing and twin density due to its coarse step size and projection on the surface, EBSD shows the same trend as high-resolution TEM-based investigations: most twins are formed under the (010)[101]track, a much smaller amount is found under the (010)[001] wear track and no twinning, but massive amounts of dislocation plasticity, occur under the (111)[$\bar{1}$10] wear track.

Because of the complex stress state under the spherical indenter, pile-up formation and dynamic nature of wear, it is difficult to determine the stress components involved in the plastic deformation during wear especially which would be responsible for twinning. Discrete dislocation dynamics (DDD) simulation studies carried out by Gagel et al. [15] show that for the same crystal normal direction, the sliding direction influences whether the dislocations are transported or not below the indenter. They observed that in FCC crystal with (010) orientation, [101] sliding direction shows significant dislocation transport while [100] sliding direction does not. The anisotropy in dislocation motion could be responsible for disparity between twin densities in our experiments. Partial dislocation glide is precursor to twin nucleation; if less dislocation motion occurs in the (010)[001] wear track, then less twins form in this loading condition than in the (010)[101]wear directions.

We did not observe any twins in the [111] grain, whether we used SEM or TEM based techniques. Therefore, we conclude that twins do not form in this grain orientation. This conclusion is supported by the DDD studies conducted by Gagel et al. [15] which demonstrate that in certain grain orientations, the slip plane is aligned parallel to the sliding direction which facilitates dislocation motion on long distances – resulting in dislocation plasticity.

4.3. Multivariant twin microstructure

Fig. 5 shows the multivariant twin microstructure consisting of at least two twin systems under the wear track in (010)[101] direction. To visualize this structure, a schematic (Fig. 12) is presented. From the TEM

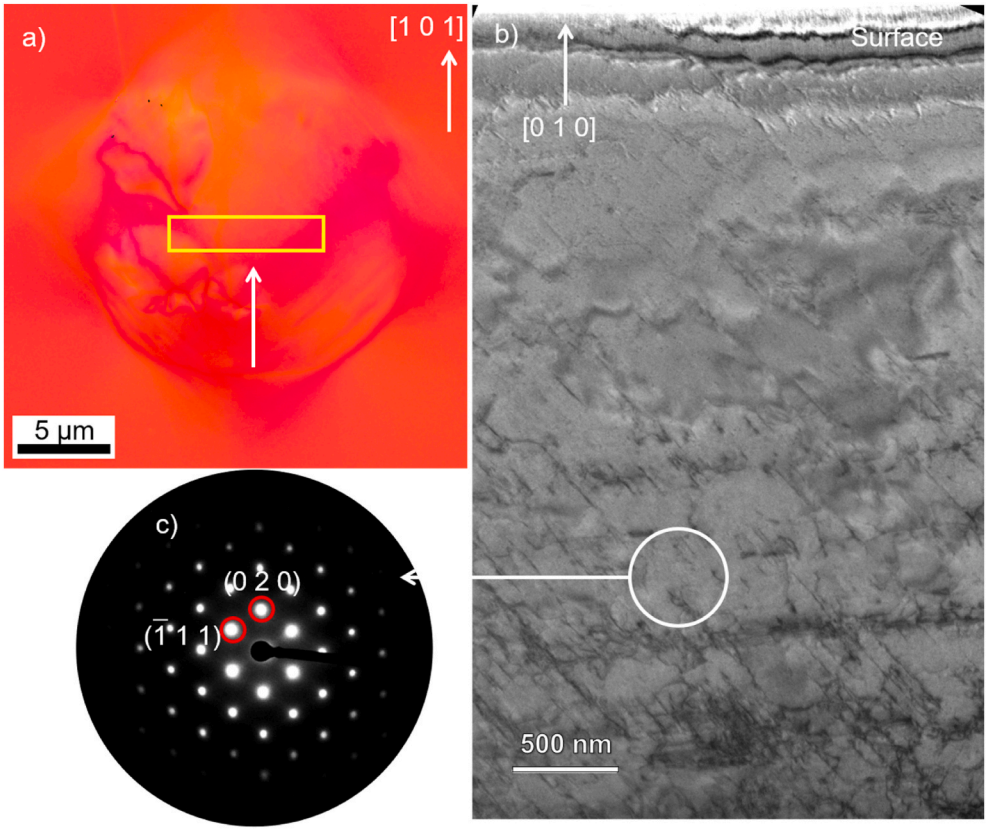

Fig. 11. a) IPF map from EBSD scan of the indent in (010) grain. b) BF-TEM image of TEM foil from the region indicated by a rectangle in a). c) Diffraction pattern from the region highlighted by a white circle in b) taken at $[101]$ zone axis.

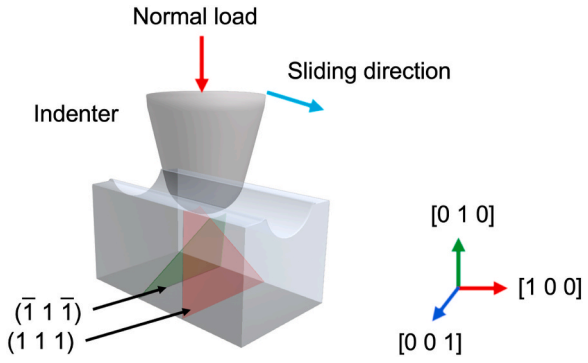

Fig. 12. Schematic drawing of multi-variant twins belonging to $(\bar{1}1\bar{1})$ and (111) twin systems below the wear track.

analysis we conclude that at least two twin systems are present from the $[10\bar{1}]$ zone axis. The twins are edge-on and they belong to the $(\bar{1}1\bar{1})$ and (111) planes while other twin systems are not edge-on and are invisible in the BF-TEM image. This type of microstructure has been observed for several FCC metals as a result of severe deformation [21].

This microstructure is a result of the high compressive and shear stress generated in the material during wear. Sliding an indenter on the surface generates large compressive shear stresses in front of the indenter tip which – among other things – result in a pile-up in front of the counter body. These compressive and shear stresses are responsible for the nucleation of twins and as the indenter slides across the surface, these twins grow and form the microstructure as displayed in Fig. 4. Fig. 5b) shows an intersection of two twin systems where the primary twin plane: $(\bar{1}1\bar{1})$ is aligned in the sliding direction and in the direction of the pile-up which forms during sliding. As these planes are perfectly aligned in the wear direction, they allow for effective deformation in the sliding direction. Contrary, the (111) plane is aligned opposite to the sliding direction and therefore do not correspond to the motion. Hence, these planes are considered secondary. Please note for dislocation plasticity, Gagel et al. [15] also observed that well aligned dislocation systems are more active than those which are not well aligned.

The twin-twin intersection and the dislocation mechanisms lead to the formation of complex microstructure has only piqued an interest in last two decades because in some cases it leads to phase transformation (formation of martensite and ε phase) and amorphization at the intersections. These interactions have promising effects on the strain hardening of a deformed metal [22–24]. We demonstrate that the twin-twin intersection in our case do not show any phase transformation, but it shows high lattice distortion at the intersection. We conclude that during scratching, the activation and formation of multivariant twin systems could be associated with inherent low stacking fault energy of material in which multiple stacking faults nucleate which become precursor to the twinning, the growth of the twins on $(\bar{1}1\bar{1})$ twin plane and conjugate twin plane (111) depends on the local stress state.

5. Conclusion

We carried out a comparative study in which the deformation mechanism during wear and indentation were identified. In addition, the effect of wear direction on the deformation anisotropy is studied.

1. The wear carried out in a (010) grain reveals twinning to be the primary mode of deformation while wear in a (111) grain reveals dislocation glide as a primary mode of deformation.
   - TEM analysis of the area under the wear tracks in the $(010)[101]$ and $(010)[001]$ direction shows that there are at least two twin

systems active in each case. Twin density and twin spacing measurements reveal that $(\bar{1}1\bar{1})$ twins are 44 ± 5 nm apart while (111) twin spacing is 20 ± 3 nm. Twins below (010)[001] wear track belong to $(\bar{1}1\bar{1})$ and $(\bar{1}\bar{1}1)$/ $(1\bar{1}\bar{1})$ twin planes. The difference in twin density is due to the inclination of the twin plane in relation to the wear direction. More twins occur if the twinning plane is in the direction of wear, hence this plane is deemed efficient than a plane against the wear direction.

- TEM analysis of the area under an indent in (010) grain shows that the deformation is predominantly by dislocation glide and shows entangled dislocation structures with a dislocation density of 9.4 ± 2.0 × $10^{13}/m^2$.
- TEM analysis under the wear track (111)[$\bar{1}$10] direction reveals an entangled dislocation structures with a dislocation density of 1.6 ± 0.8 × $10^{14}/m^2$ and with no twins. In this orientation, the dislocation systems are well aligned to accommodate plasticity and twinning is less required.

To quantify the CRSS and evaluate the 3D stress state, further analytical studies are required to understand the mechanisms behind the multiple twin microstructure and the quantification of the wear direction.

Author statement

Piyush Patil – Investigation, visualization, data curation, writing – original draft preparation.

Subin Lee – Investigation, formal analysis, writing – reviewing and editing.

Gerhard Dehm – Supervision, validation, writing – reviewing and editing.

Steffen Brinckmann – Conceptualization, Methodology, Supervision, Writing – reviewing and editing.

Declaration of competing interest

The authors declare that they have no known competing financial interests or personal relationships that could have appeared to influence the work reported in this paper.

Acknowledgement

We would like to acknowledge IMPRS-SURMAT, MPIE, Düsseldorf for providing funding for the project as well as Mr. Volker Kree, Mr. Philipp Watermayer, Mr. Leon Christiansen and Ms. Hanna Tsybenko for their help with the SEM, TEM, metallography and confocal microscopy.

Appendix A. Supplementary data

Supplementary data to this article can be found online at https://doi.org/10.1016/j.wear.2022.204403.

References

[1] A. Dalmau, C. Richard, A. Igual – Muñoz, Degradation mechanisms in martensitic stainless steels: wear, corrosion and tribocorrosion appraisal, Tribol. Int. 121 (May 2018) 167–179, https://doi.org/10.1016/j.triboint.2018.01.036.

[2] I. Tzanakis, M. Hadfield, B. Thomas, S.M. Noya, I. Henshaw, S. Austen, Future perspectives on sustainable tribology, Renew. Sustain. Energy Rev. 16 (6) (Aug. 2012) 4126–4140, https://doi.org/10.1016/j.rser.2012.02.064.

[3] K.D. Ralston, N. Birbilis, Effect of grain size on corrosion: a review, Corrosion 66 (7) (Jul. 2010), https://doi.org/10.5006/1.3462912, 075005-075005–13.

[4] Physical properties of surfaces IV—polishing, surface flow and the formation of the beilby layer, Proc. R. Soc. Lond. Ser. - Math. Phys. Sci. 160 (903) (Jun. 1937) 575–587, https://doi.org/10.1098/rspa.1937.0127.

[5] K. Lu, J. Lu, Nanostructured surface layer on metallic materials induced by surface mechanical attrition treatment, Mater. Sci. Eng., A 375 (377) (Jul. 2004) 38–45, https://doi.org/10.1016/j.msea.2003.10.261.

[6] T. Mang, K. Bobzin, T. Bartels, Industrial Tribology: Tribosystems, Friction, Wear and Surface Engineering, 2011 lubrication.

[7] C. Greiner, Z. Liu, L. Strassberger, P. Gumbsch, Sequence of stages in the microstructure evolution in copper under mild reciprocating tribological loading, ACS Appl. Mater. Interfaces 8 (24) (Jun. 2016) 15809–15819, https://doi.org/10.1021/acsami.6b04035.

[8] F.J. Humphreys, M. Hatherly, Chapter 2 - the deformed state, in: F.J. Humphreys, M. Hatherly (Eds.), Recrystallization and Related Annealing Phenomena, second ed., Elsevier, Oxford, 2004, pp. 11–II, https://doi.org/10.1016/B978-008044164-1/50006-2.

[9] M. Niewczas, Chapter 75 dislocations and twinning in face centred cubic crystals, Dislocations in Solids 13 (2007) 263–364, https://doi.org/10.1016/S1572-4859(07)80007-6. Elsevier.

[10] W. Christian and S. Mahajant, 'DEFORMATION twinning', Prog. Mater. Sci., p. 157.

[11] Y.F. Shen, X.X. Li, X. Sun, Y.D. Wang, L. Zuo, Twinning and martensite in a 304 austenitic stainless steel, Mater. Sci. Eng., A 552 (Aug. 2012) 514–522, https://doi.org/10.1016/j.msea.2012.05.080.

[12] M. Sabzi, M. Farzam, Hadfield manganese austenitic steel: a review of manufacturing processes and properties, Mater. Res. Express 6 (10) (Sep. 2019), 1065c2, https://doi.org/10.1088/2053-1591/ab3ee3.

[13] I. Karaman, H. Sehitoglu, H.J. Maier, Y.I. Chumlyakov, Competing mechanisms and modeling of deformation in austenitic stainless steel single crystals with and without nitrogen, Acta Mater. 49 (19) (Nov. 2001) 3919–3933, https://doi.org/10.1016/S1359-6454(01)00296-8.

[14] I. Karaman, H. Sehitoglu, K. Gall, Y.I. Chumlyakov, H.J. Maier, Deformation of single crystal Hadfield steel by twinning and slip, Acta Mater. 48 (6) (Apr. 2000) 1345–1359, https://doi.org/10.1016/S1359-6454(99)00383-3.

[15] J. Gagel, D. Weygand, P. Gumbsch, Discrete Dislocation Dynamics simulations of dislocation transport during sliding, Acta Mater. 156 (Sep. 2018) 215–227, https://doi.org/10.1016/j.actamat.2018.06.002.

[16] G. Meric de Bellefon, J.C. van Duysen, K. Sridharan, Composition-dependence of stacking fault energy in austenitic stainless steels through linear regression with random intercepts, J. Nucl. Mater. 492 (Aug. 2017) 227–230, https://doi.org/10.1016/j.jnucmat.2017.05.037.

[17] G. Dehm, S.H. Oh, P. Gruber, M. Legros, F.D. Fischer, Strain compensation by twinning in Au thin films: experiment and model, Acta Mater. 55 (19) (Nov. 2007) 6659–6665, https://doi.org/10.1016/j.actamat.2007.08.027.

[18] M.N. Gussev, J.T. Busby, T.S. Byun, C.M. Parish, Twinning and martensitic transformations in nickel-enriched 304 austenitic steel during tensile and indentation deformations, Mater. Sci. Eng., A 588 (Dec. 2013) 299–307, https://doi.org/10.1016/j.msea.2013.08.072.

[19] E.J. Seo, J.K. Kim, L. Cho, J. Mola, C.Y. Oh, B.C. De Cooman, Micro-plasticity of medium Mn austenitic steel: perfect dislocation plasticity and deformation twinning, Acta Mater. 135 (Aug. 2017) 112–123, https://doi.org/10.1016/j.actamat.2017.06.014.

[20] G.C. Sneddon, P.W. Trimby, J.M. Cairney, Transmission Kikuchi diffraction in a scanning electron microscope: a review, Mater. Sci. Eng. R Rep. 110 (Dec. 2016) 1–12, https://doi.org/10.1016/j.mser.2016.10.001.

[21] S. Mahajan, G.Y. Chin, Twin-slip, twin-twin and slip-twin interactions in Co-8 wt.% Fe alloy single crystals, Acta Metall. 21 (2) (Feb. 1973) 173–179, https://doi.org/10.1016/0001-6160(73)90059-X.

[22] C. Efstathiou, H. Sehitoglu, Strain hardening and heterogeneous deformation during twinning in Hadfield steel, Acta Mater. 58 (5) (Mar. 2010) 1479–1488, https://doi.org/10.1016/j.actamat.2009.10.054.

[23] H.W. Zhang, Z.K. Hei, G. Liu, J. Lu, K. Lu, Formation of nanostructured surface layer on AISI 304 stainless steel by means of surface mechanical attrition treatment, Acta Mater. 51 (7) (Apr. 2003) 1871–1881, https://doi.org/10.1016/S1359-6454(02)00594-3.

[24] S. Zhao, Q. Zhu, K. Song, H. Zhou, J. Wang, Role of intersecting grain boundary on the deformation of twin-twin intersection, Scripta Mater. 188 (Nov. 2020) 184–189, https://doi.org/10.1016/j.scriptamat.2020.07.034.